



Steering photo-excited towards active sites: Intensified substrates affinity and spatial charge separation for photocatalytic molecular oxygen activation and pollutant removal

Hanbo Yu^{a,b}, Jinhui Huang^{a,b,*}, Longbo Jiang^{a,b}, Xingzhong Yuan^{a,b,*}, Kaixin Yi^{a,b}, Wei Zhang^{a,b}, Jin Zhang^{a,b}, Haoyun Chen^{a,b}

^a College of Environmental Science and Engineering, Hunan University, Changsha 410082, PR China

^b Key Laboratory of Environment Biology and Pollution Control, Hunan University, Ministry of Education, Changsha 410082, PR China

ARTICLE INFO

Keywords:

Photocatalysis
Ciprofloxacin degradation
InVO₄
BiOBr
Facet engineering

ABSTRACT

Bismuth oxybromide-based heterostructure has been constructed widely for various photocatalytic application. However, the function of the exposed facets in heterostructure still remains to be elucidated. Herein, we chemically implanted bismuth oxybromide nano-units with dominantly exposed (010) facets on indium vanadate particles to form composites. Results showed that the absorption range of visible light was extended due to the high photosensitivity of InVO₄ and the charge transfer was also effectively expedited by the formation of internal electric field. Contrast experiments manifested that BiOBr with dominant (010) facets was more suitable than that with (001) facets to act as electron acceptor in InVO₄/BiOBr heterojunction, because the open channels on (010) facets provided large accommodation space for organic pollutants. Thus, the generated superoxide radicals on BiOBr could annihilate the adsorbed pollutants rapidly. Moreover, the hierarchical core-shell structure provided large surface area to further intensify the affinity of InVO₄/BiOBr composites to pollutants. Consequently, the hierarchical InVO₄/BiOBr heterojunction exhibited excellent photocatalytic activity and could degrade 92.59% of ciprofloxacin (CIP) within 1 h under visible light. The reaction data were fitted with multiple models to investigate the whole reaction process. Furthermore, the impacts of various simulated actual factors on CIP adsorption and degradation were explored. The intermediates and possible degradation pathways were also illustrated through Liquid Chromatography-Mass/Mass Spectrometry (LC-MS). This work not only provide a facet engineering concept for heterojunction construction, but also help us to further understand the relationship between adsorption and photocatalytic degradation.

1. Introduction

Recently, the aggravating environmental pollution and energy shortage have attracted tremendous attention worldwide. Photocatalysis technology has been considered as a promising strategy to address these issues [1–5]. Therefore, a great deal of effort has been devoted to developing efficient semiconductor photocatalysts for various applications, such as wastewater treatment [6], bacterial destruction [5], hydrogen evolution [7] and CO₂ reduction [8]. Whereas, the reality is the capability of photocatalysts is far from satisfying the practical application requirements. Two of the major issues are the limited optical absorption and the fast charge carriers recombination. Thus, seeking and constructing efficient heterogeneous

photocatalysts have become a potential strategy for improving photocatalytic activity [9–14].

Indium vanadate (InVO₄), with the band gap of about 2.3 eV, has been considered promising for visible-light driven pollutant decomposition and hydrogen evolution. Originally, the InVO₄ powders were synthesized by solid-state reaction with raw materials of In₂O₃ and V₂O₅ or In(NO₃)₃ and NH₄VO₃ [15]. In recent years, the application of solution routes gradually became the mainstream for direct synthesis of crystalline InVO₄ particles at low temperature due to its versatility in controlling the microstructure and physical properties of materials. As results, various InVO₄ morphologies, such as nanorods, nanoparticles, nanobricks and nanosheets, have been prepared through tuning environmental pH value and adding different surfactants [16]. Although the

* Corresponding authors at: College of Environmental Science and Engineering, Hunan University, Changsha 410082, PR China.

E-mail addresses: Huangjinhui@hnu.edu.cn (J. Huang), yxz@hnu.edu.cn (X. Yuan).

<https://doi.org/10.1016/j.cej.2020.127334>

Received 10 July 2020; Received in revised form 15 September 2020; Accepted 9 October 2020

Available online 15 October 2020

1385-8947/© 2020 Elsevier B.V. All rights reserved.

relatively narrow band gap and excellent chemical stability endow InVO_4 with wonderful talent as visible-light-response photocatalyst, the catalytic performance of pristine InVO_4 is still not ideal. Undoubtedly, the quick recombination of photogenerated charges is answerable for the poor photocatalytic activity. However, the limited number of active sites confined in tiny surface area is also a mainly passive factor [17–20].

Bismuth oxybromide (BiOBr) as a remarkably multi-component V–VI–VII semiconductor, has been widely used as photocatalyst due to its intrinsic superiority of self-generated internal electric fields (IEF) along (001) direction [21]. More importantly, the surface atom coordination of BiOBr could be manipulated by modulating the configuration between $[\text{Bi}_2\text{O}_2]$ units and bromine atoms, leading to the formation of distinguishing crystal facets and then exhibited different photocatalytic performances [22]. For instance, Wu et al. increased the percentage of (001) facet exposure by adding different amount of nitric acid, correspondingly leading to higher CO_2 photoreduction activity and improved inactivation of *Escherichia coli* [10,23]. Whereas, Scott's group reported that BiOBr with dominantly exposed (010) facets possessed better photo-oxidative capability for oxygen evolution and formic acid degradation [24]. Other research reported that BiOBr with dominant (010) facets exhibited better photocatalytic performance towards salicylic acid degradation than that dominated by the (001) facet under visible light ($\lambda > 420 \text{ nm}$), while the opposite was true under light wavelength of 254 nm [25]. Despite of the promoting effect of crystal facet engineering, the rapid recombination of photogenerated charges and the insufficient visible light absorption always limited the photocatalytic activity of BiOBr monomer. Therefore, lots of hybrid BiOBr-based materials with interlaced band structures have been prepared, such as AgI/BiOBr [13], Bi/BiOBr [26], g- C_3N_4 /BiOBr [27], Cu_2O /BiOBr [28], BiOBr/ NiFe_2O_4 [29] and MIL-53/BiOBr [30]. However, the influence of specific exposed facets of BiOBr in heterojunction towards photocatalytic performance has been rarely reported. Actually, the (010) facets have been demonstrated to benefit the injection of photo-induced electrons from plasmonic metals or dyes, as well as offer more active sites and broader accommodation space for the pollutants adsorption due to its open channel characteristics (Scheme S1) [31,32]. Therefore, we proposed a hypothesis that constructing InVO_4 /BiOBr heterojunction with (010) facets of BiOBr as mainly exposed surface would promote the photocatalytic activity.

Considering that three-dimensional hierarchical architectures generally display increased adsorption capacity due to the increased surface area, it is viable to construct hierarchical InVO_4 /BiOBr nanostructure to further improve the photocatalytic activity [33]. Herein, we in situ implanted unit BiOBr nanosheets with dominantly exposed (010) facets on InVO_4 nanoparticles via a novel solvothermal strategy [34], which resulted in a well-defined InVO_4 /BiOBr core-shell structure. Various characterization methods was conducted to probe into the physicochemical and photoelectrical properties. The performance of InVO_4 /BiOBr photocatalysts with different exposed facets for CIP removal was investigated under visible light irradiation ($\lambda > 420 \text{ nm}$). The adsorption and degradation results were studied with multiple models. Plenty of actual factors were selected to investigate the significance of adsorption for CIP removal. Meanwhile, the photodegradation products and pathway of CIP were investigated by the LC-MS. In virtue of the inertia of BiOBr in NIR region, the charge transfer direction and the function of active sites on BiOBr were verified. The radical trapping experiments and ESR measure were also conducted to inquire into the photodegradation mechanisms. This study proposed a new design tactic to control the exposed facets and the surface properties of heterojunction and might be helpful for understanding the photocatalytic pollutants removal mechanism.

2. Experimental section

2.1. Synthesis of InVO_4

InVO_4 nanoparticles were prepared by a PVP-assistance hydrothermal method [35]. Typically, 1 mmol $\text{In}(\text{NO}_3)_3 \cdot 4.5\text{H}_2\text{O}$ and 1 mmol NH_4VO_3 were dissolved in 40 mL deionized water under ultrasonication, respectively. After 10 min, 200 mg PVP was dispersed in the $\text{In}(\text{NO}_3)_3 \cdot 4.5\text{H}_2\text{O}$ solution and magnetically stirred for 20 min. Then the NH_4VO_3 solution was dropped into the above solution under continuous stirring and the pH value of the mixed suspension was adjusted to 6.4 with $\text{NH}_3 \cdot \text{H}_2\text{O}$. After one-hour agitation in dark environment, the obtained suspension was transferred to an 100 mL Teflon-lined stainless autoclave and maintained at 180 °C for 24 h. Afterwards, the naturally cooled product was washed for three times with ultrapure water and ethyl alcohol, respectively. Finally, the resultant InVO_4 nanoparticles were dried at 65 °C overnight for further use.

2.2. Synthesis of InVO_4 /BiOBr

The InVO_4 /BiOBr heterojunction photocatalyst was prepared by a solvothermal method. In a typical procedure, the different amount of InVO_4 were dispersed in beakers containing 20 mL 2-methoxyethanol separately under ultrasonic condition for 10 min to form a uniform suspension. Then 1 mmol $\text{Bi}(\text{NO}_3)_3 \cdot 5\text{H}_2\text{O}$ were added to the above suspensions. Simultaneously, 1 mmol $[\text{C}_{12}\text{min}]\text{Br}$ were dissolved into another 20 mL 2-methoxyethanol. After stirred for 30 min, the latter solutions were poured into the former suspensions and further stirred for 10 min. Finally, the mixtures were heated in Teflon-lined stainless steel autoclave at 160 °C for 2 h. After the solvothermal process, the targeted powders were collected through centrifugation, rinse and drying processes. The samples containing different amounts of InVO_4 were marked as IB-5, IB-10, IB-20 and IB-30, where the theoretical mass ratios of InVO_4 to BiOBr were 5%, 10%, 20% and 30%, respectively.

For comparison, pure BiOBr was fabricated by the similar procedure without the addition of InVO_4 nanoparticles. Plate-like BiOBr with dominantly exposed (001) and (010) facets and the corresponding InVO_4 /BiOBr heterojunctions were also prepared by hydrothermal method as previous reported [22]. Details were provided in [Supplementary Materials](#).

2.3. Photocatalytic degradation ability

The photocatalytic degradation activity of InVO_4 /BiOBr composite was evaluated using CIP as target pollutant under visible light irradiation. A typical batch test contained 50 mg catalyst and 10 mg L^{-1} CIP in 100 mL of solution. The visible-light source was a 300 W Xenon lamp (CEL-HXF300F3) equipped a light filter ($\lambda > 420 \text{ nm}$) to cut off UV light. The light density parameter was 37.86 mW/cm^2 , which was detected by PL-MW2000 photoradiometer. The distance between the light source and liquid level was about 16 cm and the exposed area under illumination was about 63.62 cm^2 . As a comparison, another Xenon lamp source (Beijing Perfectlight, PLS-SXE300D/300DUV) with a light filter ($\lambda > 420 \text{ nm}$) was also employed. The light density parameter was 63.13 mW/cm^2 . Prior to irradiation, the mixed solution underwent a sonication for 1 min and was stirred in dark condition for 60 min to ensure the adsorption-desorption equilibrium. At a given time interval of irradiation, 3 mL aliquot was taken out from the reactor and centrifuged. The reaction solution was analyzed by the means used in our previous report [13].

Photocatalytic generation of superoxide radical ($\cdot\text{O}_2^-$) was investigated with nitroblue tetrazolium (NBT) as indicator under visible light irradiation [36]. Refer the detailed experimental procedure in the [Supplementary Materials](#).

3. Results and discussion

3.1. Physicochemical properties

The design and fabrication of core-shell composites, composed of InVO_4 nanoparticles coated with BiOBr nanosheets was illustrated in Scheme. S2. $[\text{C}_{12}\text{min}]\text{Br}$ as an attractive bromide source could form emulsions in 2-methoxyethanol due to the limited miscibility [37]. These microsized $[\text{C}_{12}\text{min}]\text{Br}$ miniemulsions coating on InVO_4 , acted as the microreaction chambers to react with Bi^{3+} ions, which surrounded the mini-emulsions. Thus, at elevated temperature, the newly formed BiOBr nanosheets may attached onto the surface of InVO_4 with assistance of minimized surface energy. The XRD patterns of $\text{InVO}_4/\text{BiOBr}$ compounds (Fig. S1) obviously comprised two sets of diffraction peaks and the characteristic peaks of InVO_4 were linearly intensified with its increased proportion in composites, indicating the successful growth of BiOBr on the surface of InVO_4 nanoparticles. Importantly, the high intensity ratios of both (110) to (001) peaks and (200) to (002) peaks indicated that the dominant facet was (010) facets of BiOBr [21,38]. ESR spectra (Fig. S2) implied that the BiOBr possessed somewhat crystal defects due to the relatively low crystallinity, which might benefit to the photocatalytic reaction.

Zeta potential results (Fig. S3) revealed that in most cases, BiOBr and InVO_4 owned same electric charge, meaning that the formation of heterostructure was not dependent on electrostatic interaction but on chemical bonding, which was beneficial for charge transfer. XPS spectra were recorded to further investigate the formation of $\text{InVO}_4/\text{BiOBr}$ heterojunction. As displayed in Fig. S4a, all of Bi, O, Br, In and V elements coexisted in survey spectrum, indicating the formation of $\text{InVO}_4/\text{BiOBr}$ composite. In high resolution XPS spectra (Fig. S4b–e), the binding energy of Bi 4f and Br 3d decreased accompanied with the red shift of In 3d and V 2p peaks in IB-20, indicating that charge transfer occurred at the interface [39,40]. According to these results, we believed that the $\text{InVO}_4/\text{BiOBr}$ heterojunction was successfully constructed and an internal electric field (IEF) was formed.

The microscopic morphologies of the obtained samples were also characterized by SEM and TEM. InVO_4 nanoparticles mainly displayed popcorn and rod shapes with size of 200–500 nm (Fig. 1a and d). The pristine BiOBr completely showed flower-like microspheres built by interlaced BiOBr nanosheets (Fig. 1b and e). The size was estimated to be 2–3 μm . The SEM images of $\text{InVO}_4/\text{BiOBr}$ heterostructure was shown in Fig. 1c and f, in which BiOBr sheets uniformly grew on the surface of InVO_4 particles to form a core-shell structure. Compared with pure BiOBr microsphere, the size of heterostructure was decreased to

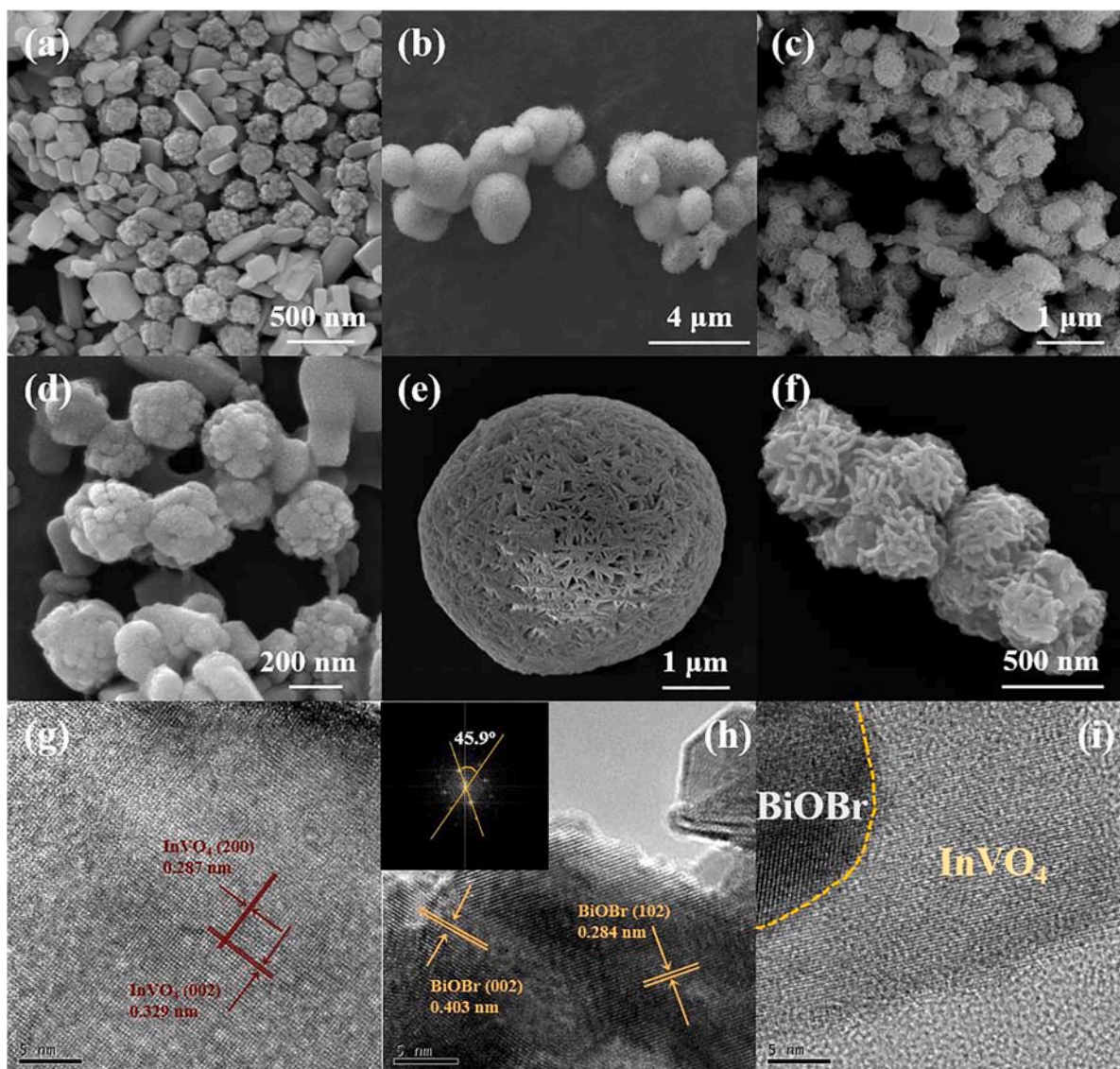


Fig. 1. The SEM images of (a and d) InVO_4 , (b and e) BiOBr and (c and f) IB-20. (d–e) the corresponding HRTEM images of them, respectively.

nanoscale, availing to the contact of photocatalysts with pollutant molecules. The EDS mapping images (Fig. S6) and HRTEM images (Fig. 1g-i) further confirmed the combination of InVO₄ with BiOBr [41,42]. It was noteworthy that two lattice fringes with spacing of 0.284 nm and 0.403 nm were observed on the surface of BiOBr (Fig. 1h), which matched well with the (102) and (002) planes, respectively [43]. The corresponding SAED pattern (inset in Fig. 1h) displayed that (102) and (002) planes formed an angle of approximately 45.9°, indicating the dominantly exposed (010) facets [22]. The result coincided with XRD. Unquestionably, InVO₄/BiOBr-(010) composites with close contact were successfully fabricated. Benefitting from the hierarchical core-shell structure, the specific surface area (Fig. S7) was enlarged (35.62 m² g⁻¹), compared with pure InVO₄ (9.82 m² g⁻¹) and pure BiOBr (29.49 m² g⁻¹). The largely exposed surface were expected to impose favorable effect on the photocatalytic efficiency [44,45].

3.2. Optical absorption and photoelectric properties

The light absorption property of the obtained photocatalysts were evaluated by the UV/vis diffuse reflectance spectra (DRS). The results showed all the samples had response under UV-vis light and incorporation of InVO₄ could improve the optical absorption ability of BiOBr within visible light region (Fig. 2a). In addition, the energy band edges (E_g) of semiconductors could be calculated by Kubelka-Munk equation (Eq. (1)) [3]:

$$ah\nu = A(h\nu - E_g)^{n/2} \quad (1)$$

where E_g was the band gap energy, A was a constant, and α , ν , h represented the absorption coefficient, Planck's constant and light frequency, respectively. Here, the values of n were determined to be 1 for InVO₄ and 4 for BiOBr according to the type of electronic transition in semiconductor [46,47]. As shown in Fig. 2b, the band gaps of as-obtained photocatalysts were confirmed to be 2.47 eV and 2.71 eV corresponding to InVO₄ and BiOBr, respectively.

Furthermore, the XPS valence band (VB XPS) spectra were also

measured to estimate the valence band (VB) edge positions of InVO₄ and BiOBr (Fig. 2c). The VB potentials of InVO₄ and BiOBr were determined to be +1.74 eV and +2.23 eV, respectively. Thus, the conduction band (CB) edge positions of InVO₄ and BiOBr were calculated to be -0.73 eV and -0.48 eV, respectively. The semiconductor type and flat band potential (U_{fb}) were characterized by Mott-Schottky (M-S). As displayed in Fig. 2d, both InVO₄ and BiOBr exhibited n-type semiconductor properties [48]. The U_{fb} of the samples were identified to be -0.48 eV and -0.13 eV vs NHE, respectively [49]. Theoretically, the CB position of n-type semiconductors is more negative about 0–0.2 V than U_{fb}, the calculated results were well in line with the previous calculated CB values.

With the aim of systematically surveying the movement action of photogenerated charges, photoelectrochemical and photoelectric measurements were performed. The transient photocurrent response curves (Fig. 2e) displayed substantial increase of photocurrent signal under visible light from IB-20, which was nearly 10 and 2 times of pure InVO₄ and BiOBr, respectively. The enhancement could be attributed to the formation of IEF between InVO₄ and BiOBr, which acted as an electron transport channel to accelerate the electron transfer. Meanwhile, pure BiOBr exhibited higher photocurrent intensity than InVO₄, even though InVO₄ possessed stronger visible light absorption ability, demonstrating that fast recombination of photoexciton severely restrained the photocatalytic ability of InVO₄. The electrochemical impedance spectroscopy (EIS) measurement further confirmed the accelerated interfacial charge migration over IB-20 (Fig. 2f). These results manifested that incorporating BiOBr with InVO₄ could not only enhance the optical absorption ability but also achieve giant enhancement on charge separation efficiency.

3.3. Photocatalytic performance

The as-synthesized IB-x samples with different InVO₄ mass ratios were investigated for the CIP removal under visible light irradiation to determine their capabilities for water purification. Fig. 3a showcased

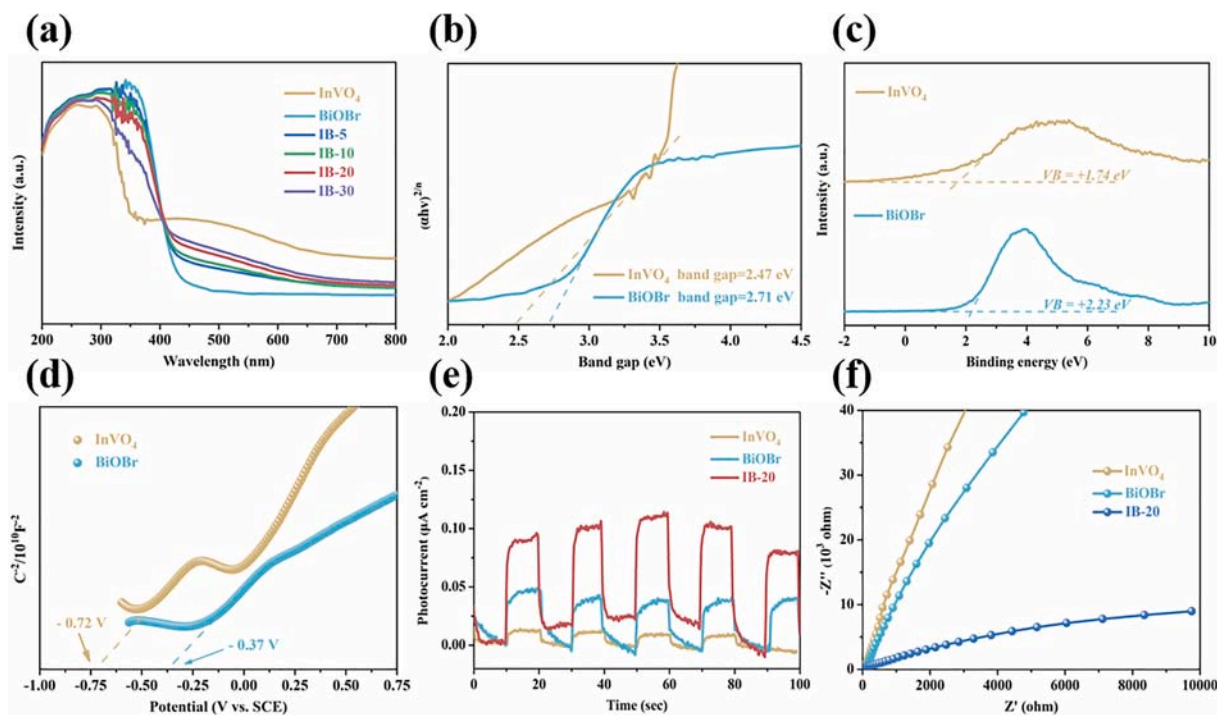


Fig. 2. (a) UV-vis absorption spectra over InVO₄, BiOBr and IB-x samples; (b) the plots of the transformed Kubelka-Munk function $(\alpha h\nu)^{n/2}$ vs. the absorbed photon energy ($h\nu$), (c) XPS valence band spectra and (d) the Mott-Schottky plots of pure InVO₄ and BiOBr; (e) transient photocurrent response of pristine InVO₄, BiOBr and IB-20; (f) corresponding EIS Nyquist plots of the prepared composites.

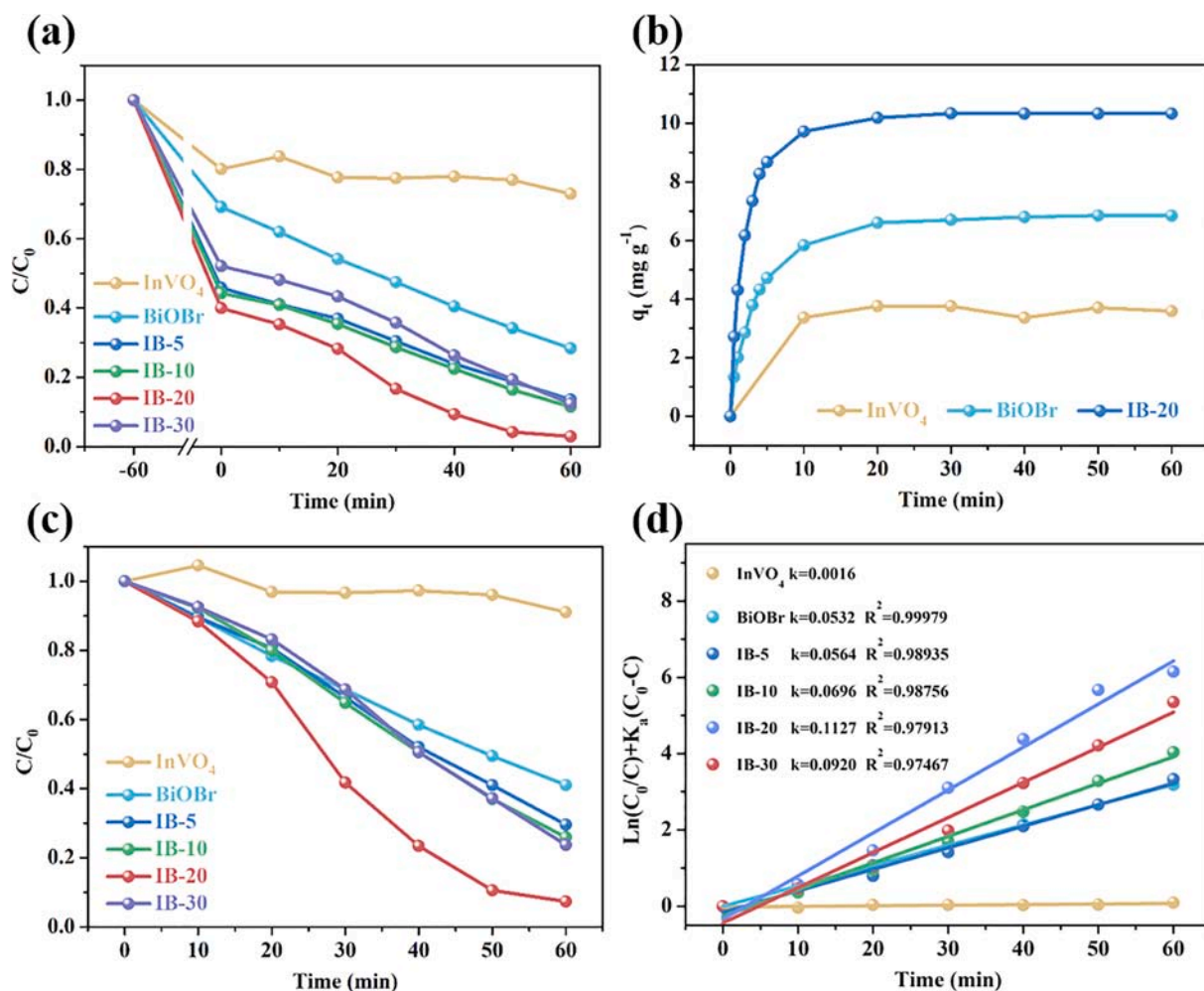


Fig. 3. (a) The total removal curves of different samples; (b) adsorption effect of as-prepared samples toward CIP in dark condition; (c) photocatalytic activities and (d) the corresponding reaction kinetic curves of as-obtained samples under visible light.

the total CIP concentration changes vs. adsorption or irradiation time in the presence of the as-prepared photocatalysts. About 27.04% and 71.63% of CIP was removed in the whole 120 min of reaction (60 min adsorption and 60 min visible light irradiation) over pure InVO₄ and pure BiOBr, respectively, and the removal efficiencies increased after coupling InVO₄ with BiOBr. The optimal removal rate appeared on IB-20, where 97.04% of CIP was dislodged from the solution.

It was noted that the IB-x samples had much higher adsorption ability than pure InVO₄ and pure BiOBr, which might be an important factor that affected the following photocatalytic degradation. In order to eliminate the distraction of adsorption effect on the experiment data in light stage, the adsorption tests of above samples for CIP were carried out under the dark conditions. As depicted in Fig. 3b, all of the photocatalysts could reach their saturation adsorptions within 60 min, indicating that the adsorption process wouldn't affect the accuracy of the following photocatalysis results. IB-20 owned much higher adsorption quantity than BiOBr, which was attributed to the enlarged surface area. Furthermore, the adsorption curves were fitted with pseudo-first-order equation and pseudo-second-order equation, respectively and the results were listed in Fig. S8. Pseudo-second-order kinetics process was more suitable for our data and the rate constants were determined to be 0.1391 g min⁻¹ mg⁻¹ and 0.0943 g min⁻¹ mg⁻¹ for BiOBr and IB-20, respectively. This result illustrated that chemical adsorption was the rating-limiting step in the adsorption process [50]. Afterwards, Langmuir and Freundlich adsorption isotherm models were employed to interpret the adsorbent-adsorbate interaction, respectively. As shown in

Fig. S9, the Langmuir isotherm model correlated better than Freundlich isotherm model for BiOBr and IB-x samples, whose R² were greater than 0.99. It was suggested that the monolayer adsorption of CIP occurred [51]. Meanwhile, the adsorption coefficient K_a were calculated based on the fitted Langmuir isotherm curves and listed in the nested table in Fig. S9a.

Furthermore, the photocatalytic degradation of CIP over different photocatalysts was investigated. As shown in Fig. 3c, there was no significant reduction in the concentration of CIP in the presence of a single InVO₄ after 60 min of visible light irradiation. BiOBr displayed relatively higher activity with decomposition efficiency of 58.93%. However, the photocatalytic CIP degradation efficiency of IB-x composites was remarkably higher than that of single InVO₄ and single BiOBr, indicating that InVO₄ played a significant role in the photocatalytic degradation although it had no CIP degradation activity. Moreover, it was also found that the CIP degradation efficiency depended, to a large extent, on the incorporation content of InVO₄. Obviously, the photodegradation efficiency improved as the InVO₄ content rose from 5 wt% to 20 wt%. Importantly, the IB-20 composite exhibited the optimal outcome, where 92.59% of CIP was decomposed within 60 min. However, the further increment of InVO₄ content from 20 wt% to 30 wt% lead to an attenuation in photocatalytic degradation, which was due to the fact that the excessive InVO₄ might adhere onto the surface of BiOBr shell and blocked the pores, suppressing the exposure of reactive sites. It was interesting to note that there was a lag on the degradation curves of IB-x composites within the first 20 min after switching on the light. This

strange photocatalytic performance might be caused by the vast adsorption quantities under dark condition, which was further discussed in the following part.

The degradation kinetics was fitted by pseudo-first-order model as displayed in Fig. S10a. Although the order of reaction rate constants was consistent with the degradation efficiencies, the pseudo-first order model seemed inadequate to fit the CIP degradation over BiOBr and IB-x samples. Meanwhile, we observed that the degradation data in the first 20 min well fitted for the zero-order kinetic rate equation with relatively low rate constants and the measured data after 20 min transformed to be in good relation to the first-order kinetic rate equation with relatively high rate constants (Fig. S10b). Actually, adsorption of the organic pollutant molecules on the surface of photocatalysts could be an important factor that affected the photocatalytic degradation rate. After dark reaction, the surface of photocatalysts tended to be saturated with adsorbed CIP molecule. Thus, in the first 20 min, the generation of active oxidation species would be the rate-limiting and preferentially attacked the already adsorbed CIP. When achieving the adsorption-degradation equilibrium, pollutant molecules in solution could swimmingly attach to the surface of photocatalyst, leading to a first-order kinetic reaction. This phenomenon was similar with the previous reported work [51]. Fortunately, another equation (Eq. (2)) based on Langmuir-Hinshelwood model, which considered the adsorption was proposed [52].

$$\frac{1}{K_a} \ln \left(\frac{C_0}{C} \right) + (C_0 - C) = k_r t \quad (2)$$

where C (mg L^{-1}) and C_0 (mg L^{-1}) were the concentration of CIP at reaction time t and initial time under irradiation condition; k_r ($\text{mg L}^{-1} \text{min}^{-1}$) was the reaction rate constant. As depicted in Fig. 3d, the degradation data were fitted quite well and the degradation rate of IB-20 was almost 2.12 and 70.44 times that of BiOBr and InVO_4 , respectively. The comparisons of photocatalytic degradation efficiency towards CIP over recently reported photocatalysts were listed in Table S4. As can be seen, the performance of IB-20 was relatively conspicuous, despite various reaction conditions including dosage, light density and incident wavelength.

The stability and repeatability of the obtained photocatalysts are very important in the practical water purification. To evaluate their stabilities, the IB-20 composite was used in cycling experiments and the results were shown in Fig. 4a. There was still an excellent removal capacity for CIP after four repeated treatments, where the CIP degradation efficiency was 83.79% on the fifth cycling run, slightly lower than that of

the initial round (92.59%). Moreover, XRD of the fresh and used IB-20 composited were provided to detect the robustness of the crystal structures. As shown in Fig. 4b, the XRD pattern of the used IB-20 had no significant distinction compared with the original one, which suggested that the crystalline structure had no changes before and after reaction.

In order to deeply investigate the CIP degradation, total organic carbon (TOC) measurements was employed. As shown in Fig. S11, IB-20 photocatalyst showed great mineralization capacity (TOC removal rate) of 71.88% to CIP under visible light irradiation, which was much dazzling than that of pristine BiOBr (37.81%). In order to probe into the potential second pollution, the LC-MS technique was carried out to identify the main intermediate products and the total MS spectra of possibly molecular intermediates at different reaction time were listed in Figs. S12 and S13. Apparently, plenty of degraded products appeared as prolonging the reaction time and the peak intensities of all intermediates performed extremely low, which proved the exclusion of organic carbon by the photocatalytic effort of $\text{InVO}_4/\text{BiOBr}$ composites. Meanwhile, the proposed structural formulas of the primary chemical components in mass spectra were listed in Table S2. According to the data analysis and relevant literatures [53,54], the reasonable degradation pathways of CIP were proposed, as illustrated in Scheme 1. In summary, three plausible pathways were involved in the decomposition of CIP. Pathway 1: CIP \rightarrow P1 (m/z 362) \rightarrow P2 (m/z 334) \rightarrow P3 (m/z 306) \rightarrow P4 (m/z 291) \rightarrow P5 (m/z 263) \rightarrow P6 (m/z 245) \rightarrow P7 (m/z 274). In this degradation process, one dominant product of the desethylene ciprofloxacin (P3) was detected due to a net loss of $-\text{C}_2\text{H}_2$ at the piperazinyl substituent of CIP, where the N (1) and N (4) atoms in the piperazine ring could be easily attacked by h^+ so that the piperazine ring opening was initially happened to form dialdehyde derivative P1 and subsequently lost one formaldehyde to form keto-derivatives P2 and P2', then the other formaldehyde was eliminated leading to the formation of P3. Further oxidation of P3 imposed the generation of P4 with a keto group through the loss of amine nitrogen. After decarbonylation, the aniline (P5) was produced, in which the piperazinyl ring of CIP was completely destroyed. Then, the subsequent defluorination and oxidation transformed P5 to P7. Pathway 2: CIP \rightarrow P9 (m/z 348) \rightarrow P10 (m/z 320) \rightarrow P11 (m/z 318). This pathway mainly involved the cleavage of the quinolone ring. Firstly, CIP was attacked by hydroxyl radicals, generating hydroxylation intermediate P9. After decarboxylation and hydroxylation, P10 was formed. Finally, followed by F substitution and quinolone ring opening, an opened ring product P11 formed. Pathway 3: CIP \rightarrow P8 (m/z 330). In this pathway, the photo-substitution of the F atom by $-\text{OH}$ was first occurred. Although the subsequently detailed intermediates were too plethoric to

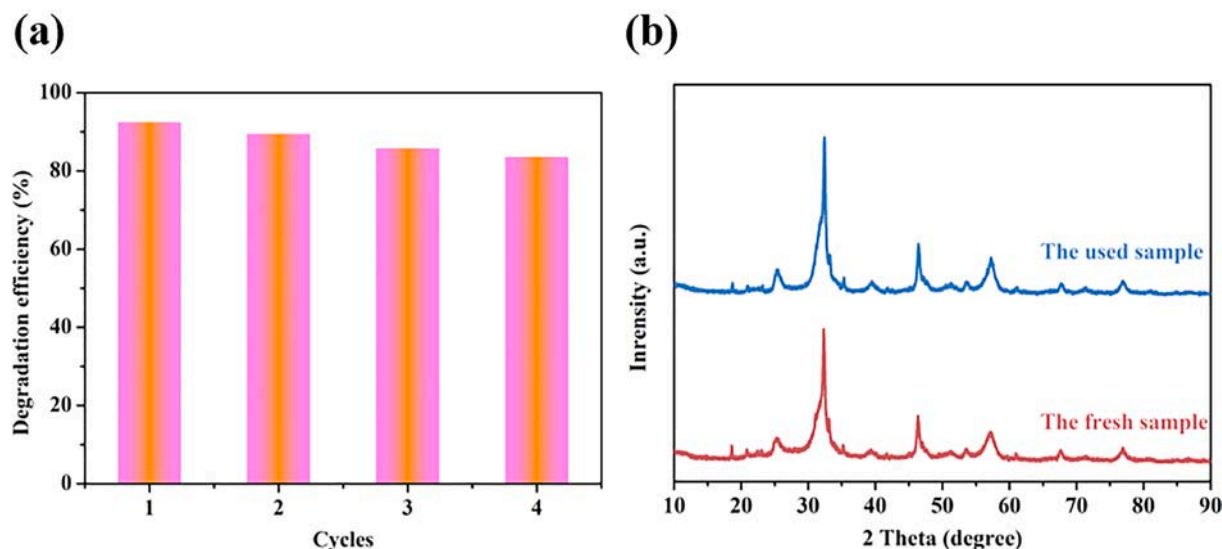
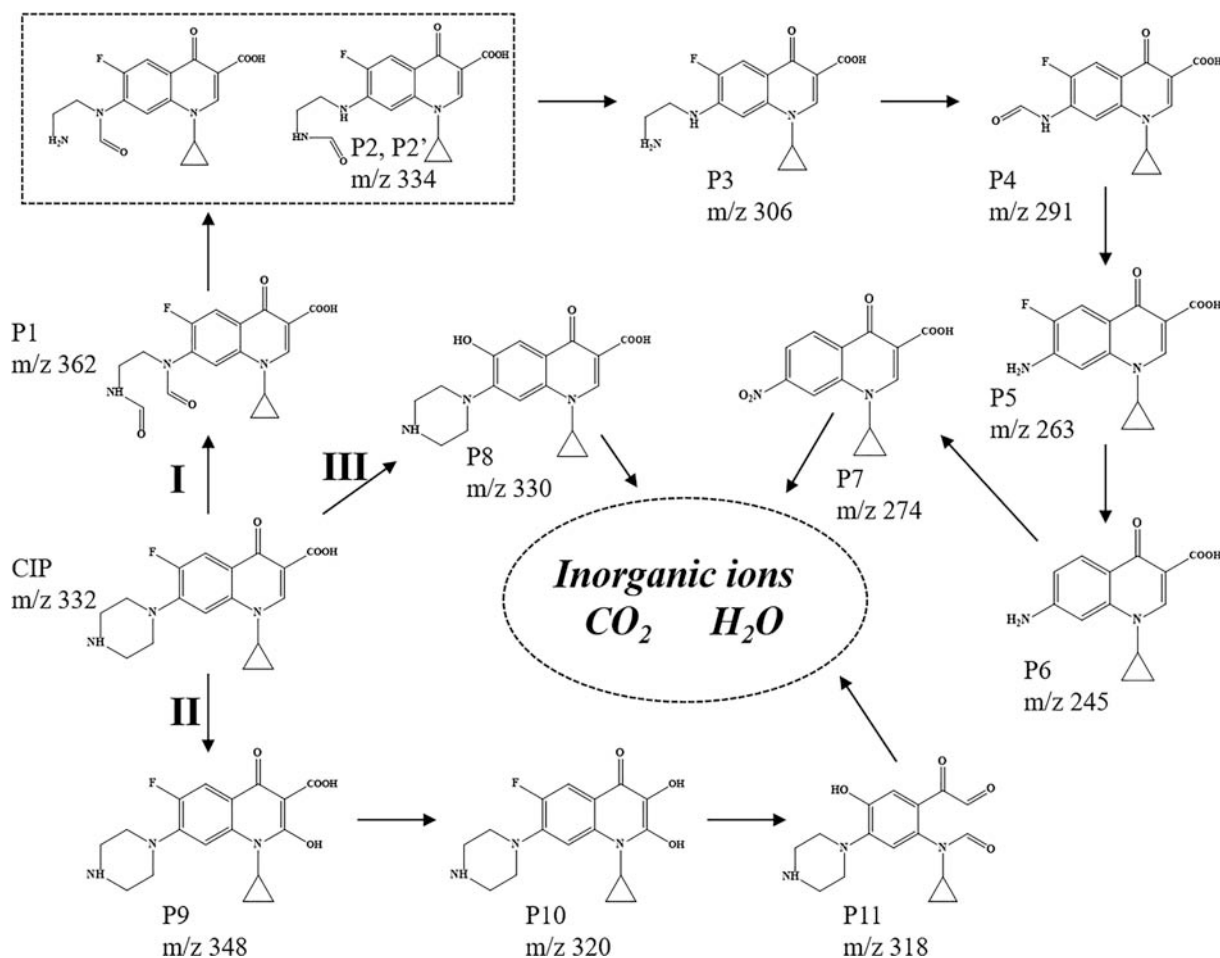


Fig. 4. (a) Recycling runs of IB-20 for degradation of CIP; (b) XRD spectra of IB-20 before and after photocatalytic reactions.



Scheme 1. Suggested photocatalytic degradation pathway of CIP.

be identified, the depressed peak intensity in MS spectra evidently confirmed the further cleavage of P8. According to the TOC tests, all of the byproducts could be further mineralized into elemental molecular substances or even CO_2 and H_2O .

In order to assess the feasibility of applying IB-20 to degrade CIP via photocatalysis in real waters, three water matrices in the environment were selected. As a benchmark, deionized water was also included. Fig. 5a displayed the effects of these water matrices on the degradation of CIP over the time period of 60 min. The degradation efficiencies at 60 min were decreasing in the order of deionized water (92.59%), underground water (87.69%), river water (75.40%) and tap water (62.60%). Therefore, compared to deionized water, the degradation of CIP was inhibited in environmental waters, but the IB-20 photocatalyst in underground water and river water still remained appreciable removal performances. Notably, the degradation efficiency in tap water was unexpectedly the worst one and the degradation trends in these three natural water matrices were different from that in deionized water, which was likely a result of the multiple action of many factors, involving solution pH value, inorganic ion species as well as the dissolved organic substance. Thus, the following sections will study the impacts in detail.

The influence of pH on the IB-20 mediated degradation of CIP was evaluated, as shown in Fig. 5b. When the pH values were within the range of 5–9, the IB-20 composites maintained high degradation efficiencies, which showed an up trend with the augmentation of pH value. Whereas only 20.08% and 39.88% were removed at the pH of 3 and 11, respectively. The free-fall decline might be related with the surface properties of photocatalyst and the states of CIP molecules. As known, different pH value may lead to the alterations in Zeta potential of

catalysts and the transformation of ciprofloxacin speciation via the protonation-deprotonation reaction [4,55]. The CIP molecule can form five molecular species including CIP^{3+} species ($\text{pH} < 3.01$), CIP^{2+} species ($3.01 < \text{pH} < 6.14$), CIP^+ species ($6.14 < \text{pH} < 8.70$), CIP^- species ($8.70 < \text{pH} < 10.58$) and CIP^{2-} species ($\text{pH} > 10.58$) as shown in Fig. S14a. It was clear that the pH value of 10.58 acted as a boundary to distinguish the states of CIP molecules, where the lower pH value endowed the CIP molecules with positive charge and vice versa the CIP molecules exhibited negative charge at the pH value above 10.58. Meanwhile, the Zeta potentials of IB-20 at different pH conditions were investigated in Fig. S14b. When the pH was in the range of 3–9, the surface of IB-20 presented positive charges with an approximately downward trends, where the electrostatic repulsion between IB-20 and the protonated CIP tended to be weaker. Thus, the amount of CIP molecules attached to the active sites on the surface of IB-20 was enlarged, which was in favor of the photocatalysis. Nevertheless, the Zeta potential chopped to -22.8 mV at pH value of 11, implying that the repulsive force between IB-20 and the deprotonated CIP was intensified and thereby led to an inferior CIP degradation efficiency. The adsorption experiment well evidenced this phenomenon as shown in Fig. S14c. The increased pH value gave rise to a gradual increment on the adsorption percentage in the range of 3 to 9 and a drastic shrink occurred at the pH 11. Considering that strong acid or alkaline environment might corrode the structure of BiOBr, the solubility of Bi ion with pH value was tested by ICP-MS as shown in Fig. S14d. The relatively high leaching amount indicated that the strong acid would injure the BiOBr crystal, which was another potential reason for the declined degradation ability at pH 3.

Considering that tap water was the most-affected water matrix for the degradation of CIP, the impacts of the commonly contained

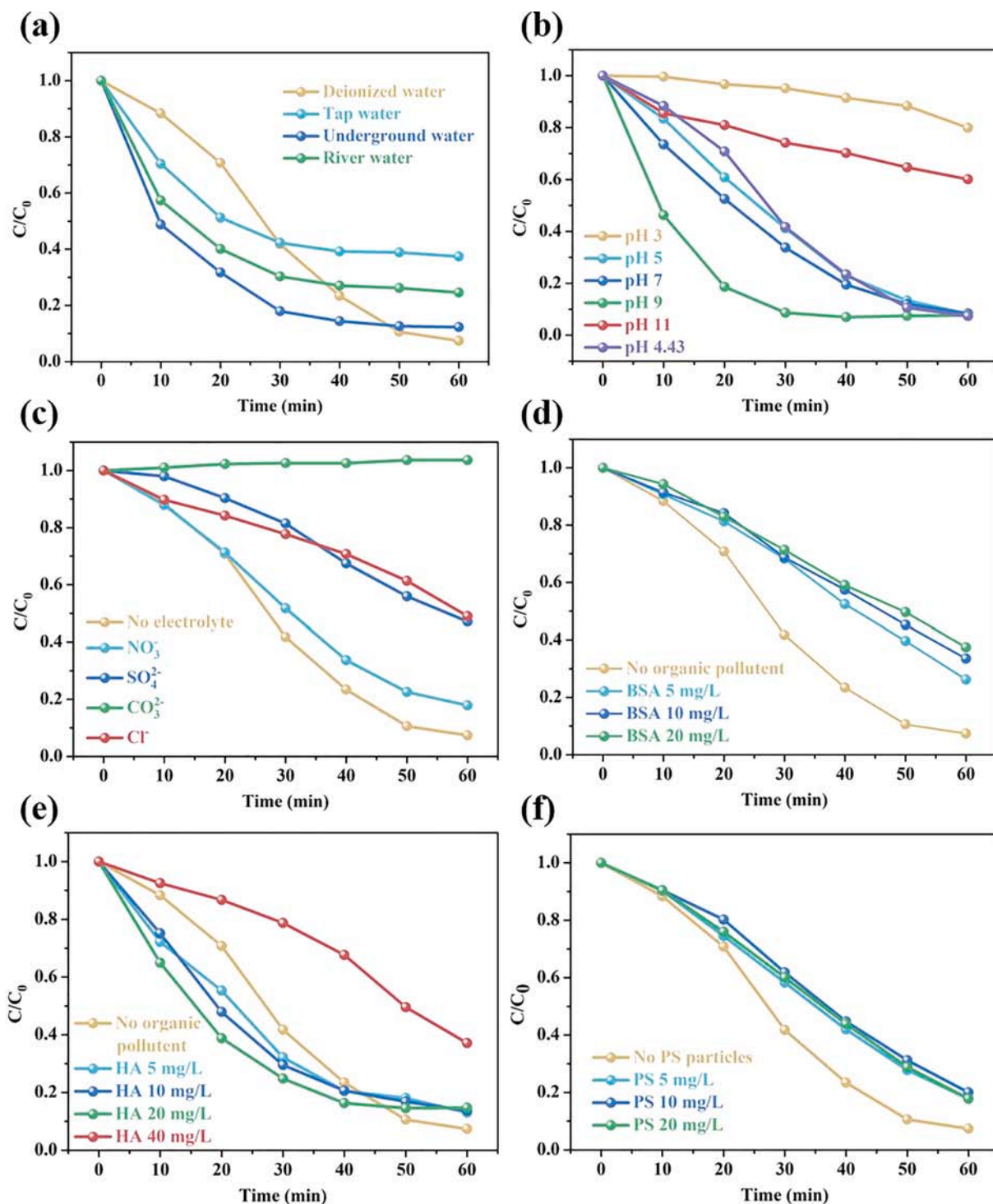


Fig. 5. Effects of different (a) water matrices, (b) pH values, (c) inorganic salts, (d) BSA, (e) HA and (f) polystyrene (PS) particles upon the removal of CIP by IB-20.

inorganic anions (Cl^- , NO_3^- , SO_4^{2-} and CO_3^{2-}) were systematically evaluated. The unadjusted solution (pH 4.43) was employed, and the selected ions (NaCl , NaNO_3 , Na_2SO_4 and Na_2CO_3) were added separately to the ciprofloxacin solution at concentrations of 50 mM. As Fig. 5c showed, no significant decay could be seen in the degradation curve of the solutions containing NaNO_3 , indicating that NO_3^- did not impact the degrading activity of IB-20 composite. However, the presence of NaCl , Na_2SO_4 and Na_2CO_3 inhibited the degradation process obviously and the photocatalyst in Na_2CO_3 even was inactivation. Due to the fact that the surface of IB-20 in neutral solution was electropositive, these anions

may prefer to adhere to the photocatalyst, which covered some active sites and changed the surface charge of material as shown in Table S3. Furthermore, Cl^- may cause the BiOBr transform to BiOCl which adsorbed poor visible light, and CO_3^{2-} could be hydrolyzed to produce a certain amount of OH^- ions and HCO_3^- ions, which increased the pH value of solution (from 4.3 to 10.4) and quenched some active species [56]. Therefore, moderate pretreatment was necessary in the treatment of the wastewater with extreme pH or sulfite, carbonate and chloride anions.

Ciprofloxacin typically coexists with natural dissolved organic

matters in natural water and wastewater. Accordingly, bovine serum albumin (BSA) and humic acid (HA) were chosen as representatives to investigate the effects of the coexisting organic substances on the CIP degradation. Fig. 5d indicated that the removal efficiency of CIP was significantly restrained by the addition of BSA regardless of concentration. This may be induced by the competitive interaction of BSA with the oxidized radicals. And the hydrophobic binding interaction and van der Waals forces between CIP and BSA also played an important role in the reduced photocatalytic performance [57]. As shown in Fig. S15a, the adsorption amount of CIP on the surface of IB-20 was reduced dramatically with the increase of BSA corresponding to the gradually deteriorative degradation performance. Furthermore, Fig. 5e showed that, up to a point relatively lower concentrations of HA (5 mg/L–20 mg/L) accelerated the CIP removal rate compared to that without HA. However, the higher concentration of 40 mg/L cut down the degradation efficiency from 92.59% to 62.89%. This phenomenon was triggered by the fact that HA as a photosensitizer could be excited to $^3\text{HA}^*$ states that promoted the formation of reactive species or induced the degradation of CIP via energy transferring [58]. However, excessive HA might serve as radical scavenger and light filter [59]. Meanwhile, HA could restrain the contact between CIP and IB-20 (Fig. S15b), thereby attenuating CIP

photocatalysis.

Microplastics which originate from the fragmentation of plastic debris or from direct environmental emission, are ubiquitous in terrestrial and aquatic environments [60]. Thus, in this study, polystyrene (PS) particles were added into the reaction system with high concentration (Fig. 5f). Interestingly, the degradation efficiency displayed a collective decline, indicating that IB-20 was not appropriate for the purification of waste water from plastics industry. Moreover, the effective prescription must be found to limit microplastics in the environment in case certain environmental treatments lose efficacy. Similarly, the adsorption percentage of CIP over IB-20 in the presence of PS particles was also measured in Fig. S15c, in which the adsorption ability of IB-20 was diminished expressively. Given that the nasty photocatalytic performances in various conditions were relevant with poor adsorption capacities, a conclusion could be proposed that the adsorption of CIP over $\text{InVO}_4/\text{BiOBr}$ composites played a vital role in the photo-degradation process.

3.4. Photocatalytic mechanism

Radical species trapping experiments were carried out to detect the

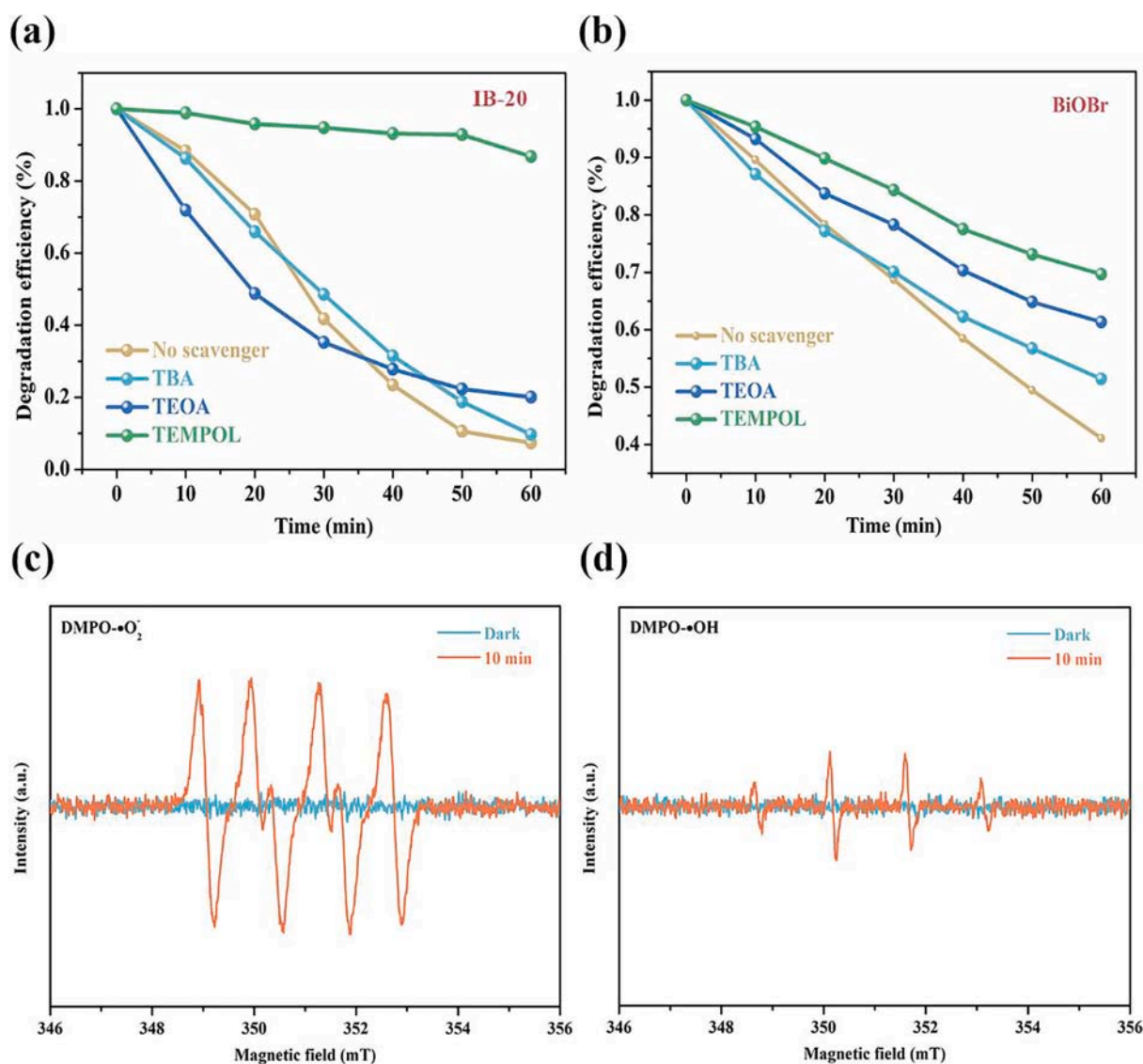


Fig. 6. Scavenger experiments of the photocatalytic degradation under visible light irradiation over (a) IB-20 and (b) BiOBr; (c and d) ESR spectra of DMPO spin-trapping over IB-20 under visible light irradiation.

generated reactive species in photocatalytic CIP degradation. 2,2,6,6-tetramethylpiperidine-1-oxyl (TEMPO), *tert*-Butanol (TBA) and Triethanolamine (TEOA) were used as scavengers of superoxide radical ($\cdot\text{O}_2^-$), hydroxyl radical ($\cdot\text{OH}$) and hole (h^+), respectively [61]. From Fig. 6a, the photodegradation activity of IB-20 displayed negligible variation after adding the TBA and TEOA, while the presence of TEMPO showed obvious inactivation effect on IB-20 catalyst, which demonstrated that $\cdot\text{O}_2^-$ was the major reactive specie in the photodegradation of CIP. It was necessary to ask a question. Did the formation of heterojunction between InVO_4 and BiOBr alter the contributions of reactive radicals? To unveil this question, the radical species trapping experiments over pure BiOBr were also conducted. As shown in Fig. 6b, the main reactive species participated in the photodegradation reaction were $\cdot\text{O}_2^-$ and h^+ , coincident with that of IB-20. However, the inhibiting effect of TEOA was stronger and the inhibiting effect of TEMPO was weaker compared to the trapping experiments over IB-20, indicating that the contributions of h^+ was decreased and the contribution of $\cdot\text{O}_2^-$ was increased after constructing $\text{InVO}_4/\text{BiOBr}$ heterojunction. The ESR signals further verified the generation of $\cdot\text{O}_2^-$ and $\cdot\text{OH}$ during the photocatalytic process (Fig. 6c and d). However, at the same illumination point-in-time (10 min), the signal intensity of DMPO- $\cdot\text{O}_2^-$ was much stronger than DMPO- $\cdot\text{OH}$, suggesting that the $\cdot\text{O}_2^-$ was the major reactive radical, and the $\cdot\text{OH}$ only played a minor role. Meanwhile, the yield of $\cdot\text{O}_2^-$ between BiOBr and IB-20 was compared in Fig. S16. The intensity of

characteristic absorption peak over IB-20 significantly declined after photocatalytic reaction and the IB-20 photocatalyst exhibited much more affinity to NBT than pure BiOBr. As a result, the total $\cdot\text{O}_2^-$ productions of BiOBr and IB-20 samples were estimated to be 7.97 and 16.41 μM after visible light irradiation for 60 min, respectively.

The steady-state and time-resolved transient photoluminescence decay spectra in Fig. 7a and b implied that the agile charge transfer between BiOBr and InVO_4 was a main reason for the promoted generation of reactive radicals. However, the contribution of the changed surface properties also should not be ignored. To identify the effect of (010) facets of BiOBr within the hierarchical structure, the photocatalytic activities of BiOBr and IB-20 with (001) facets and (010) facets were evaluated under the same condition. As shown in Fig. S17a, BiOBr-010h owned larger adsorption quantity than BiOBr-001h, indicating that the open channel on (010) facets facilitated the adsorption of organic pollutants. The hierarchical BiOBr with dominantly exposed (010) facets possessed further improved adsorption capacity, resulting from the large surface area. Meanwhile, BiOBr-010h and the corresponding heterojunction (IB-20-010h) displayed better degradation performances than those with dominant (001) facets (Fig. S17b). This suggested that the dominantly exposed (010) facets of BiOBr were more favorable to the degradation of CIP. Resultantly, the hierarchical IB-20 had much higher degradation efficiencies due to the further enlarged exposure of (010) facets. The function of (010) facets were further

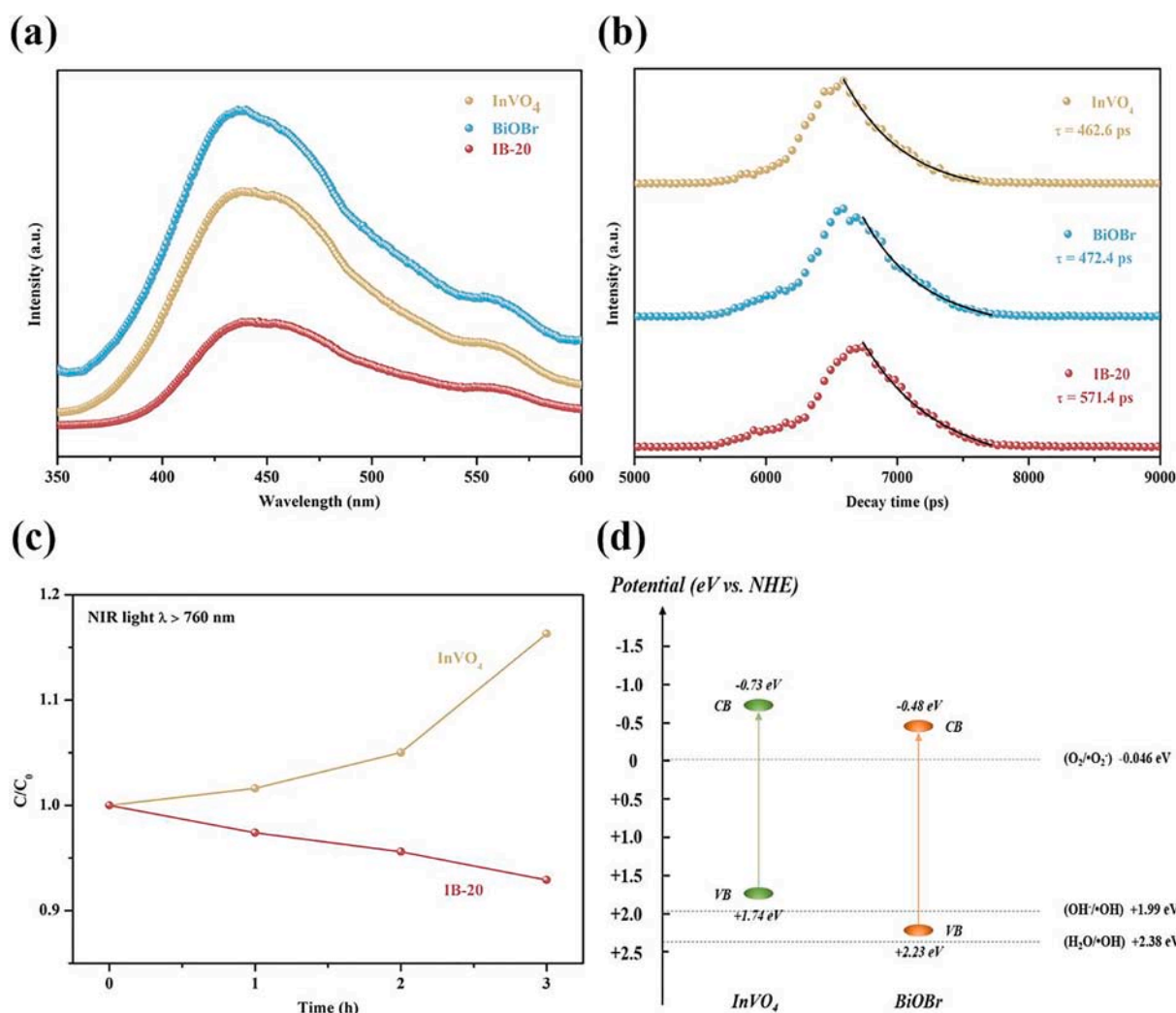


Fig. 7. (a and b) The steady-state PL spectra and ns-level time-resolved PL decay spectra of the as-prepared samples, respectively; (c) photocatalytic activities of pure InVO_4 and IB-20 photocatalysts under NIR light irradiation; (d) schematic diagram revealing the band positions of InVO_4 and BiOBr.

confirmed by the photocatalysis experiment under near-infrared (NIR) light irradiation. In terms of DRS results, only InVO_4 could absorb the light energy with wavelength longer than 760 nm and pure BiOBr was powerless under NIR region. As shown in Fig. 7c, InVO_4 could hardly remove CIP despite its NIR response ability. This phenomenon was mainly stemmed from the lack of active sites on InVO_4 surface and the rapid recombination of photoinduced charge carriers. After loading BiOBr nanosheets onto InVO_4 , the CIP concentration followed a down trend with prolonging the irradiation time, indicating that BiOBr provided extra active sites for InVO_4 .

Based on the above experimental results and the energy levels of InVO_4 and BiOBr (Fig. 7d), a photocatalytic mechanism illustrating the high-efficiency photocatalytic CIP removal over IB-20 was proposed in Fig. 8. The smaller BiOBr nanosheets with dominantly exposed (010) facets were evenly immobilized on the surface of InVO_4 by chemical bonding. Compared with BiOBr microspheres, the teeny-weeny InVO_4 particles as substrate material resulted in the smaller size of $\text{InVO}_4/\text{BiOBr}$ composites, thereby the relatively higher surface-volume ratio made more adsorption sites of BiOBr be exposed. This gave preference to CIP molecules to be adsorbed onto the surface of BiOBr in the dark. Under visible-light irradiation, both InVO_4 and BiOBr could be activated into excited state and produced electrons and holes. Considering the band positions, the CB potentials of InVO_4 and BiOBr were calculated to be -0.73 eV and -0.48 eV and their corresponding VB potentials were $+1.74$ eV and $+2.23$ eV, respectively. Therefore, the photo-produced electrons on the CB of InVO_4 could thermodynamically migrate to the CB of BiOBr whereas holes transferred oppositely in the VB due to the built-in electric field at the interface. Therefore, the photoexcited electrons and holes were effectively separated in micro-space. Furthermore, these extraneous electrons could migrate promptly on the (010) surface of BiOBr owing to the intra-electric field along (010) direction, thereby dispensing with travelling across the bulk. The existence of crystal defect might also contribute to the electron transport. Due to the CB potentials of BiOBr being more negative than the reduction potential of O_2/O_2^- (-0.33 eV vs. NHE) [4], the accumulated electrons on the CB of BiOBr could reduce molecule oxygen to generate O_2^- for CIP degradation. However, referring to the VB potential of InVO_4 which was less positive than the $\text{H}_2\text{O}/\text{OH}$ potential ($+2.38$ eV vs. NHE) [62], the holes

possessed relatively weaker oxidizability, thereby unable to oxidize H_2O into OH . That was the reason of the fact that the contribution of O_2^- was enlarged. The $\text{DMPO}\cdot\text{OH}$ signals in ESR test was probably ascribed to the further transition of O_2^- via $\text{O}_2^- \rightarrow \text{H}_2\text{O}_2 \rightarrow \text{OH}$ [20]. Coincidentally, the adsorption of CIP and the generation of active species together proceeded on BiOBr . Therefore, the O_2^- could oxidize CIP molecule quickly.

4. Conclusion

In summary, BiOBr nanosheets with different exposed facets were in situ grown on InVO_4 nanoparticles. It was demonstrated that (010) facets of BiOBr possessed larger adsorption capacity and higher degradation ability towards CIP than (001) facets, because the open channels on (010) facets provided large accommodation space for organic pollutants. Base on this, a hierarchical $\text{InVO}_4/\text{BiOBr}$ heterojunction with mainly exposed BiOBr -(010) facets was constructed. The nanometer-scale InVO_4 particles minified the size of composites, thereby achieving a much higher surface area. Consequently, the adsorption of CIP was further improved. Benefiting from the formation of internal electric field, the photogenerated charges were able to flow directionally with a prolonged lifetime. Coincidentally, the reduction of molecule oxygen was also occurred on BiOBr . Thus, the generate O_2^- could annihilate CIP as soon as possible. Deservedly, the photocatalytic reaction was accelerated. The prepared IB-20 composites presented 97.04% removal efficiency after one-hour adsorption in dark and another one-hour visible light irradiation. In addition, it also presented outstanding mineralization capability with TOC removal efficiency of 71.88% within two-hour visible light irradiation. The photocatalytic degradation pathways of CIP were deduced aided by LC-MS. Furthermore, the $\text{InVO}_4/\text{BiOBr}$ composites possessed good reusability. This work may provide a new strategy to design heterojunction photocatalyst, which gathers the pollutant adsorption and the free radicals generation on one component, to shorten the distance between radicals with target pollutants.

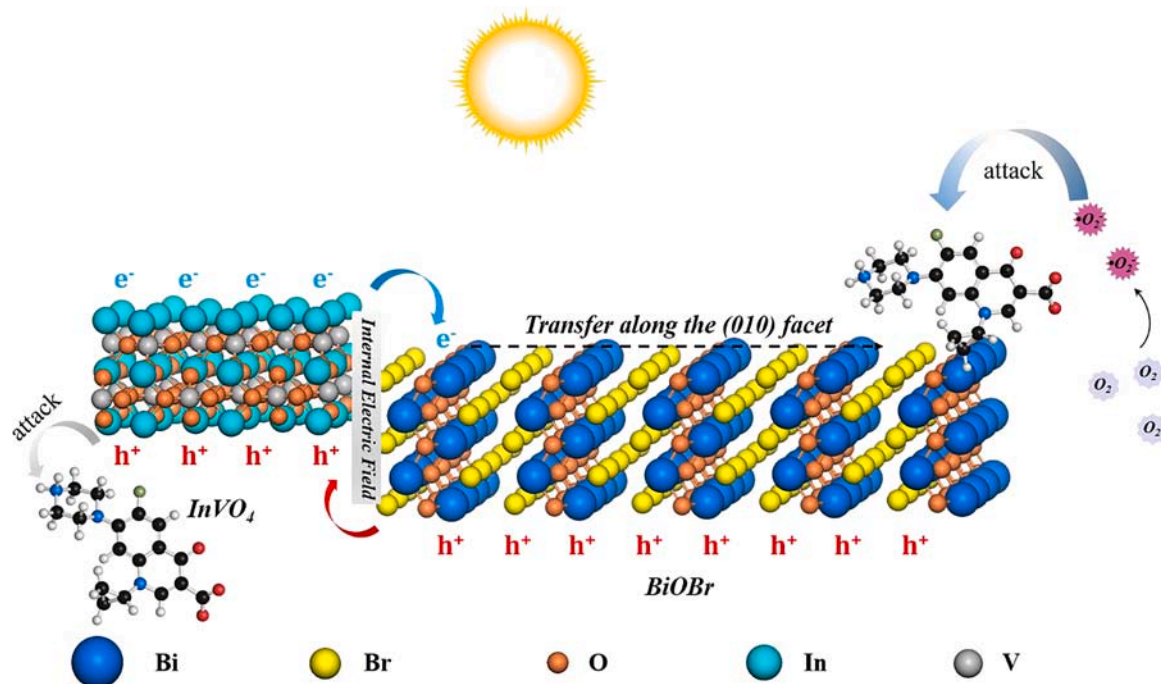


Fig. 8. Photocatalytic degradation mechanism scheme of $\text{InVO}_4/\text{BiOBr}$ photocatalyst under visible light irradiation.

Declaration of Competing Interest

The authors declare that they have no known competing financial interests or personal relationships that could have appeared to influence the work reported in this paper.

Acknowledgement

This study was financially supported by the National Natural Science Foundation of China (21776066, 51739004, 51578222 and 51521006).

Appendix A. Supplementary data

Supplementary data to this article can be found online at <https://doi.org/10.1016/j.cej.2020.127334>.

References

- [1] L. Jiang, X. Yuan, G. Zeng, J. Liang, Z. Wu, H. Wang, J. Zhang, T. Xiong, H. Li, *Environ. Sci. Nano* 5 (2018) 2604–2617.
- [2] L. Jiang, X. Yuan, G. Zeng, J. Liang, Z. Wu, H. Yu, D. Mo, H. Wang, Z. Xiao, C. Zhou, *J. Colloid Interface Sci.* 536 (2019) 17–29.
- [3] X. Yuan, L. Jiang, J. Liang, Y. Pan, J. Zhang, H. Wang, L. Leng, Z. Wu, R. Guan, *G. Zeng, Chem. Eng. J.* 356 (2019) 371–381.
- [4] W. Wang, P. Xu, M. Chen, G. Zeng, C. Zhang, C. Zhou, Y. Yang, D. Huang, C. Lai, M. Cheng, L. Hu, W. Xiong, H. Guo, M. Zhou, *ACS Sustain. Chem. Eng.* 6 (2018) 15503–15516.
- [5] W. Wang, Z. Zeng, G. Zeng, C. Zhang, R. Xiao, C. Zhou, W. Xiong, Y. Yang, L. Lei, Y. Liu, D. Huang, M. Cheng, Y. Yang, Y. Fu, H. Luo, Y. Zhou, *Chem. Eng. J.* 378 (2019), 122132.
- [6] W. Wang, Q. Niu, G. Zeng, C. Zhang, D. Huang, B. Shao, C. Zhou, Y. Yang, Y. Liu, H. Guo, W. Xiong, L. Lei, S. Liu, H. Yi, S. Chen, X. Tang, *Appl. Catal. B* 273 (2020), 119051.
- [7] X. Peng, L. Ye, Y. Ding, L. Yi, C. Zhang, Z. Wen, *Appl. Catal. B* 260 (2020), 118152.
- [8] X. Wang, S. Wang, N. Yang, W. Zhou, P. Wang, K. Jiang, S. Li, H. Song, X. Ding, H. Chen, J. Ye, *Appl. Catal. B* 259 (2019), 118088.
- [9] H. Li, J. Shang, Z. Ai, L. Zhang, *J. Am. Chem. Soc.* 137 (2015) 6393–6399.
- [10] D. Wu, L. Ye, H.Y. Yip, P.K. Wong, *Catal. Sci. Technol.* 7 (2017) 265–271.
- [11] J. Guo, X. Liao, M.-H. Lee, G. Hyett, C.-C. Huang, D.W. Hewak, S. Mailis, W. Zhou, Z. Jiang, *Appl. Catal. B* 243 (2019) 502–512.
- [12] J. Di, J. Xia, M. Ji, B. Wang, S. Yin, Q. Zhang, Z. Chen, H. Li, *Appl. Catal. B* 183 (2016) 254–262.
- [13] H. Yu, B. Huang, H. Wang, X. Yuan, L. Jiang, Z. Wu, J. Zhang, G. Zeng, *J. Colloid Interface Sci.* 522 (2018) 82–94.
- [14] H. Yu, L. Jiang, H. Wang, B. Huang, X. Yuan, J. Huang, J. Zhang, G. Zeng, *Small* 15 (2019), e1901008.
- [15] L. Zhang, H. Fu, C. Zhang, Y. Zhu, *J. Solid State Chem.* 179 (2006) 804–811.
- [16] L. Chen, Y. Liu, Z. Lu, D. Zeng, *J. Colloid Interface Sci.* 295 (2006) 440–444.
- [17] H. Liu, L. Li, C. Guo, J. Ning, Y. Zhong, Y. Hu, *Chem. Eng. J.* 385 (2020), 123929.
- [18] H. Liu, S. Ma, L. Shao, H. Liu, Q. Gao, B. Li, H. Fu, S. Fu, H. Ye, F. Zhao, J. Zhou, *Appl. Catal. B* 261 (2020), 118201.
- [19] Y. Shi, J. Huang, G. Zeng, W. Cheng, H. Yu, Y. Gu, L. Shi, K. Yi, *J. Colloid Interface Sci.* 531 (2018) 433–443.
- [20] J. Huang, J. Hu, Y. Shi, G. Zeng, W. Cheng, H. Yu, Y. Gu, L. Shi, K. Yi, *J. Colloid Interface Sci.* 541 (2019) 356–366.
- [21] Y. Mi, H. Li, Y. Zhang, N. Du, W. Hou, *Catal. Sci. Technol.* 8 (2018) 2588–2597.
- [22] M. Shi, G. Li, J. Li, X. Jin, X. Tao, B. Zeng, E.A. Pidko, R. Li, C. Li, *Angew. Chem.* 59 (2020) 6590–6595.
- [23] D. Wu, B. Wang, W. Wang, T. An, G. Li, T.W. Ng, H.Y. Yip, C. Xiong, H.K. Lee, P. K. Wong, *J. Mater. Chem. A* 3 (2015) 15148–15155.
- [24] X. Wu, Y.H. Ng, L. Wang, Y. Du, S.X. Dou, R. Amal, J. Scott, *J. Mater. Chem. A* 5 (2017) 8117–8124.
- [25] H. Li, T. Hu, N. Du, R. Zhang, J. Liu, W. Hou, *Appl. Catal. B* 187 (2016) 342–349.
- [26] F. Cao, J. Wang, Y. Wang, J. Zhou, S. Li, G. Qin, W. Fan, *Nanoscale Adv.* 1 (2019) 1124–1129.
- [27] L. Ye, J. Liu, Z. Jiang, T. Peng, L. Zan, *Appl. Catal. B* 142–143 (2013) 1–7.
- [28] W. Cui, W. An, L. Liu, J. Hu, Y. Liang, *J. Hazard. Mater.* 280 (2014) 417–427.
- [29] X. Li, L. Wang, L. Zhang, S. Zhuo, *Appl. Surf. Sci.* 419 (2017) 586–594.
- [30] L. Tang, Z.-Q. Lv, Y.-C. Xue, L. Xu, W.-H. Qiu, C.-M. Zheng, W.-Q. Chen, M.-H. Wu, *Chem. Eng. J.* 374 (2019) 975–982.
- [31] J. Jiang, K. Zhao, X. Xiao, L. Zhang, *J. Am. Chem. Soc.* 134 (2012) 4473–4476.
- [32] J. Li, X.a. Dong, Y. Sun, W. Cen, F. Dong, *Appl. Catal. B* 226 (2018) 269–277.
- [33] R. Li, H. Ren, W. Ma, S. Hong, L. Wu, Y. Huang, *Catal. Commun.* 106 (2018) 1–5.
- [34] X.-X. Wei, B. Cui, X. Wang, Y. Cao, L. Gao, S. Guo, C.-M. Chen, *CrystEngComm* 21 (2019) 1750–1757.
- [35] J. Hu, D. Chen, N. Li, Q. Xu, H. Li, J. He, J. Lu, *Appl. Catal. B* 236 (2018) 45–52.
- [36] H. Yu, J. Huang, L. Jiang, Y. Shi, K. Yi, W. Zhang, J. Zhang, H. Chen, X. Yuan, *Chem. Eng. J.* 402 (2020), 126187.
- [37] H. Cheng, B. Huang, Z. Wang, X. Qin, X. Zhang, Y. Dai, *Chemistry* 17 (2011) 8039–8043.
- [38] L. Sun, L. Xiang, X. Zhao, C.-J. Jia, J. Yang, Z. Jin, X. Cheng, W. Fan, *ACS Catal.* 5 (2015) 3540–3551.
- [39] Z.-F. Huang, J. Song, X. Wang, L. Pan, K. Li, X. Zhang, L. Wang, J.-J. Zou, *Nano Energy* 40 (2017) 308–316.
- [40] C. Feng, Y. Deng, L. Tang, G. Zeng, J. Wang, J. Yu, Y. Liu, B. Peng, H. Feng, *J. Wang, Appl. Catal. B* 239 (2018) 525–536.
- [41] Q. Han, X. Bai, Z. Man, H. He, L. Li, J. Hu, A. Alsaedi, T. Hayat, Z. Yu, W. Zhang, J. Wang, Y. Zhou, Z. Zou, *J. Am. Chem. Soc.* 141 (2019) 4209–4213.
- [42] J. Chaisorn, K. Wetchakun, S. Phanichphant, N. Wetchakun, *Mater. Lett.* 160 (2015) 75–80.
- [43] X.Y. Kong, W.P.C. Lee, W.-J. Ong, S.-P. Chai, A.R. Mohamed, *ChemCatChem* 8 (2016) 3074–3081.
- [44] H. Wang, X. Yuan, H. Wang, X. Chen, Z. Wu, L. Jiang, W. Xiong, G. Zeng, *Appl. Catal. B* 193 (2016) 36–46.
- [45] L. Jiang, X. Yuan, G. Zeng, Z. Wu, J. Liang, X. Chen, L. Leng, H. Wang, H. Wang, *Appl. Catal. B* 221 (2018) 715–725.
- [46] X. Zhang, Y. Zhang, J. Yu, Y. Zhang, Z. Cui, Y. Sun, B. Hou, *Appl. Catal. B* 220 (2018) 57–66.
- [47] Y. Guo, H. Huang, Y. He, N. Tian, T. Zhang, P.K. Chu, Q. An, Y. Zhang, *Nanoscale* 7 (2015) 11702–11711.
- [48] J. Ding, Z. Dai, F. Qin, H. Zhao, S. Zhao, R. Chen, *Appl. Catal. B* 205 (2017) 281–291.
- [49] H. Huang, B. Dai, W. Wang, C. Lu, J. Kou, Y. Ni, L. Wang, Z. Xu, *Nano Lett.* 17 (2017) 3803–3808.
- [50] T. Xiao, Z. Tang, Y. Yang, L. Tang, Y. Zhou, Z. Zou, *Appl. Catal. B* 220 (2018) 417–428.
- [51] C. Tian, H. Zhao, H. Sun, K. Xiao, P. Keung Wong, *Chem. Eng. J.* 381 (2020), 122760.
- [52] X.Z. Li, H. Liu, L.F. Cheng, H.J. Tong, *Environ. Sci. Technol.* 37 (2003) 3989–3994.
- [53] L. Li, X. Zheng, Y. Chi, Y. Wang, X. Sun, Q. Yue, B. Gao, S. Xu, *J. Hazard. Mater.* 383 (2020), 121211.
- [54] J. Deng, Y. Ge, C. Tan, H. Wang, Q. Li, S. Zhou, K. Zhang, *Chem. Eng. J.* 330 (2017) 1390–1400.
- [55] Z. Qiang, C. Adams, *Water Res.* 38 (2004) 2874–2890.
- [56] Y. Lin, S. Wu, C. Yang, M. Chen, X. Li, *Appl. Catal. B* 245 (2019) 71–86.
- [57] U. Anand, L. Kurup, S. Mukherjee, *Phys. Chem. Chem. Phys.* 14 (2012) 4250–4258.
- [58] S. Jiao, S. Zheng, D. Yin, L. Wang, L. Chen, *Chemosphere* 73 (2008) 377–382.
- [59] X. Zhu, Y. Wang, D. Zhou, *J. Soils Sediments* 14 (2014) 1350–1358.
- [60] A.A. de Souza Machado, W. Kloas, C. Zarfl, S. Hempel, M.C. Rillig, *Glob. Change Biol.* 24 (2018) 1405–1416.
- [61] Y. Yang, C. Zhang, D. Huang, G. Zeng, J. Huang, C. Lai, C. Zhou, W. Wang, H. Guo, W. Xue, R. Deng, M. Cheng, W. Xiong, *Appl. Catal. B* 245 (2019) 87–99.
- [62] Y. Shi, J. Huang, G. Zeng, W. Cheng, J. Hu, L. Shi, K. Yi, *Chemosphere* 230 (2019) 40–50.